ACS OMEGA

Open Access

http://pubs.acs.org/journal/acsodf

Article

Recyclable and Efficient Recovery of Ca and S from Phosphogypsum by Using Multistep Precipitation

Yuqian Zhou, Yuhe Zhou, Renlong Liu,* Guocan Zheng, Changyuan Tao, and Benjun Xi

Cite This: *ACS Omega* 2024, 9, 4664−4672

Read Online

ACCESS | Metrics & More | Article Recommendations

ABSTRACT: The resource utilization of phosphogypsum (PG) is the key to promote the green development of the phosphorus chemical industry. The natural environment and public safety are significantly threatened by the enormous volume of PG storage. In this study, Ca and S were successfully recovered from the PG via a multistep precipitation in the NaOH−$BaCO_3$ system. The alkali solution can be recycled five times, with a first recovery ratio of about 97.9%, and the decomposition ratio of PG remained above 70% after five cycles. In addition, the recovery ratios of Ca and S in PG are 99.9 and 82.5%, respectively. The product of $BaSO_4$ can be used as a weighting agent for oil and natural gas drilling mud. The $BaSO_4$ can also be used as wave-absorbing materials, and its reflection loss value reaches 97.8% of the analytical purity $BaSO_4$. This work provides a new idea for the efficient recycling of Ca and S in PG with an outstanding application prospect.

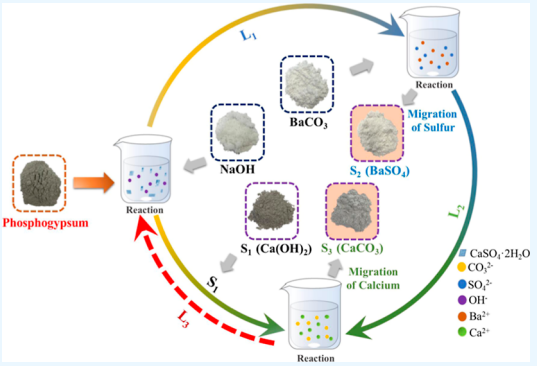

1. INTRODUCTION

The industrial solid-waste phosphogypsum (PG) is produced during the wet process of producing phosphoric acid by decomposing phosphate rock with sulfuric acid.[1] $CaSO_4{\cdot}nH_2O$ (n = 0, 1.5, 2) is the primary constituent of PG, with F, P, Si, organic material, and some metal impurities like Fe, Mg, and Al.[2] Some also contain naturally occurring radioactive elements.[3] The large-scale utilization of PG is seriously restricted by its complex composition. Therefore, it is urgent to study new methods for resource utilization of PG.

The current utilization rate of PG in China is approximately 40%. Massive amounts of PG represent a major threat to the environment.[4] At present, research on resource utilization of PG primarily focuses on the following aspects: preparing coproduced sulfuric acid cements,[5] preparation of wall materials,[6] soil conditioner,[7] and preparation of high-strength gypsum,[8] chemical raw materials,[9] modified absorption materials,[10] and so on.[11] In addition, it is used to absorb CO_2 in order to prepare $CaCO_3$.[12] This approach is beneficial for recovering Ca in PG and absorbing CO_2 from the atmosphere, but it overlooks the abundant S. The methods used in many studies are thermal decomposition, thermal reduction decomposition,[13] dissolution recrystallization,[14] hydrothermal method,[15] and dehydration rehydration, and so on.[16] However, with low consumption, high costs, and high energy consumption, the current PG utilization technology is still too immature for industrial use, and the bulk of the methods are still in the laboratory. So, other key technologies to consume PG on a large scale are still needed to further improve the resource utilization of PG.

The precipitation method has the advantages of wide sources of chemicals, low price, simple operation, and reliable treatment. Onoda et al.[17] selectively precipitated neodymium phosphate from an aqueous solution of iron−neodymium mixture to separate neodymium and iron without the use of high temperature or specialized equipment. Liu et al.[18] removed and recovered fluoride and phosphate by the stepwise precipitation method, which not only achieved the efficient removal and recovery of F and P but also separated them. Shu et al.[19] used carbonate and struvite precipitation to separate manganese and ammonia nitrogen from the leachate of electrolytic manganese residue. Interestingly, the K_{sp} values of $CaSO_4$, $BaCO_3$, $Ca(OH)_2$, $CaCO_3$, and $BaSO_4$ are 4.93×10^{-5},[20] 2.58×10^{-9},[21] 5.02×10^{-6},[22] 2.8×10^{-9},[23] and 1.08×10^{-10},[20] respectively. According to the solubility product rule, PG and $BaCO_3$ can be converted into $BaSO_4$ and $CaCO_3$ by multistep precipitation. Therefore, exploring processes for preparing $BaSO_4$ and $CaCO_3$ by the precipitation method from PG has become an interesting research topic.

In this study, a multistep precipitation method was proposed to recover Ca and S from PG in the NaOH−$BaCO_3$ system, and Ca and S were fixed as $CaCO_3$ and $BaSO_4$, respectively.

Received: October 10, 2023
Revised: December 15, 2023
Accepted: January 4, 2024
Published: January 16, 2024

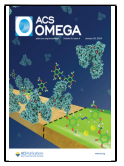

https://doi.org/10.1021/acsomega.3c07912
ACS Omega 2024, 9, 4664−4672

The filtrate from the final step is rich in OH^- and can be reused for further leaching. On the basis, a reaction between PG with filtrate recycling is proposed. Meanwhile, the reaction conditions were further optimized using the response surface and single-factor experiments, and the effects of different circumstances on the recovery of Ca and S were investigated. This study can provide a new perspective and method for PG resource development.

2. MATERIALS AND METHODS

2.1. Materials. In this study, pristine PG with tabular morphology from Hubei Province, China was used (Figure 1a), and $CaSO_4{\cdot}2H_2O$ is the main phase (Figure 1b). The

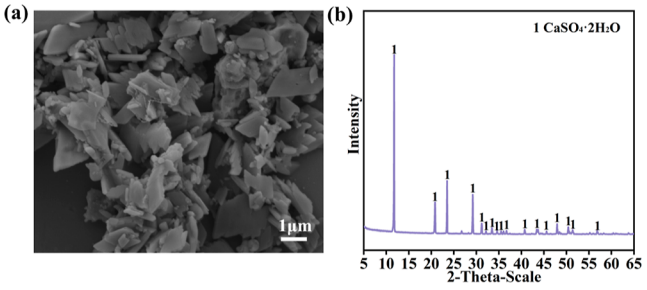

Figure 1. (a) Scanning electron microscopy (SEM) image of PG and (b) X-ray diffraction (XRD) pattern of PG.

composition of the pristine PG is listed in Table 1 in detail, with the constituents of CaO and SO_3 were major. Prior to the experiment, the PG was crushed to less than 75 μm. NaOH and $BaCO_3$ were of chemical-grade purity and purchased from Aladdin. Deionized water was used in all experiments.

2.2. Methods. The whole reaction element migration and reaction scheme are demonstrated in Figure 2. PG reacts with a certain concentration of NaOH solution to obtain solid 1 (S_1) and liquid 1 (L_1), and then, L_1 reacts with $BaCO_3$ to obtain precipitations solid 2 (S_2) and liquid 2 (L_2). Finally, L_2 reacts with S_1 to obtain precipitations solid 3 (S_3) and liquid 3 (L_3), and L_3 can be recycled with the newly added PG. The specific experimental steps are as follows:

1 Leaching with NaOH: the pretreated PG is added to the NaOH solution according to a certain ingredient ratio ($m_{(NaOH)}$:$m_{(PG)}$ = 0.44, 0.46, 0.48, 0.50, and 0.52 g/g) and liquid−solid ratio ($m_{(H_2O)}$:$m_{(PG)}$ = 3.0, 3.5, 4.0, 4.5, and 5.0 mL/g). A magnetic stirrer was used to ensure adequate mixing throughout the reaction. The mixture was heated in a water bath to maintain the desired reaction temperature. After leaching for a period of time, the filtrate was collected by vacuum and the residue was dried in an oven at 60 °C for further use. Indicate the solid and liquid as S_1 and L_1, respectively.
2 Preparation of $BaSO_4$: $BaCO_3$ (determined from the SO_4^{2-} content in L_1) was added to the L_1 obtained in step 1 under stirring condition, adjusting of different reaction temperatures and reaction times. At the end of the reaction, the precipitate was then filtered and collected and subsequently dried in an oven at 60 °C. Indicate the solid and liquid as S_2 and L_2, respectively.
3 Preparation of $CaCO_3$: a certain content of S_1 was added to the L_2 obtained in step 2 under stirring condition, adjusting of different reaction temperatures and reaction times during the reaction. At the end of the reaction, the subsequent steps are the same as in (2) and indicate the solid and liquid as S_3 and L_3, respectively. Then, the pretreated PG is added to the L_3 according to the optimal conditions obtained in step 1. The precipitate was then filtered and collected for demonstrating recyclability.

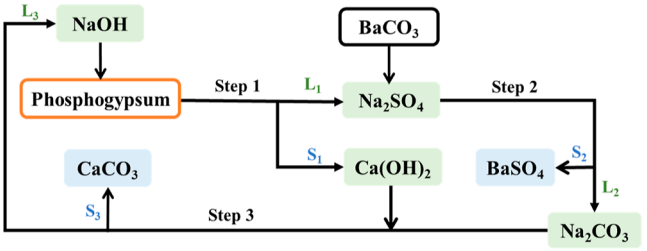

Figure 2. Overall diagrammatic drawing of the phosphogypsum recovery process.

2.3. Analytical Methods. The composition of the sample was detected by X-ray fluorescence (XRF, ARL Perform'X, Thermo Fisher Scientific CDLtd, Switzerland). Samples and precipitates were analyzed by an X-ray diffractometer (D/MAX-2500, Rigaku, Japan). Microscopic surface morphology and microscale composition analyses were conducted by using SEM (Ultra Plus, Carl Zeiss, Germany) and X-ray energy-dispersive spectroscopy (EDS, Oxford X-MAX, Carl Zeiss, Germany). Ion chromatography (IC, ICS6000, ThermoFisher Scientific, Germany) and and inductively coupled plasma atomic emission spectrometer (ICP-OES, ICAP6300, Thermo-Fisher Scientific, Britain) were used to measure the SO_4^{2-} and Ca^{2+} concentrations. Chemical titration was used to assess the amounts of CO_3^{2-} and OH^- in accordance with DZ/T 0064.49-2021. Chemical titration was used to assess the amounts of $Ca(OH)_2$ in accordance with GB/T 27815-2011, and the $CaCO_3$ content was assessed. The vector network analyzer (E5071C, Agilent, America) was used to examine the electromagnetic characteristics of the precipitations and determine the reflection loss value.

The recovery of Ca and S was estimated according to the concentrations of ions in the solution before and after the reaction. Thus, the recovery ratio of Ca^{2+} and SO_4^{2-} was determined according to the following eq 1

$$w_{(Ca^{2+}/SO_4^{2-})} = \frac{C_0 - C_1}{C_0} \times 100\% \quad (1)$$

where C_0 (g/L) is the concentration of calcium and sulfur in the initial PG solution and C_1 (g/L) is the concentration of Ca^{2+} in L_3 and SO_4^{2-} in L_2.

Table 1. Composition of the Pristine PG (wt %)[a]

component	CaO	SO_3	SiO_2	P_2O_5	Al_2O_3	MgO	Fe_2O_3	other
content	37.47	48.65	9.13	0.82	0.63	0.20	0.41	2.69

[a]Note: the chemical elements in the pristine PG are in the form of oxide.

https://doi.org/10.1021/acsomega.3c07912
ACS Omega 2024, 9, 4664−4672

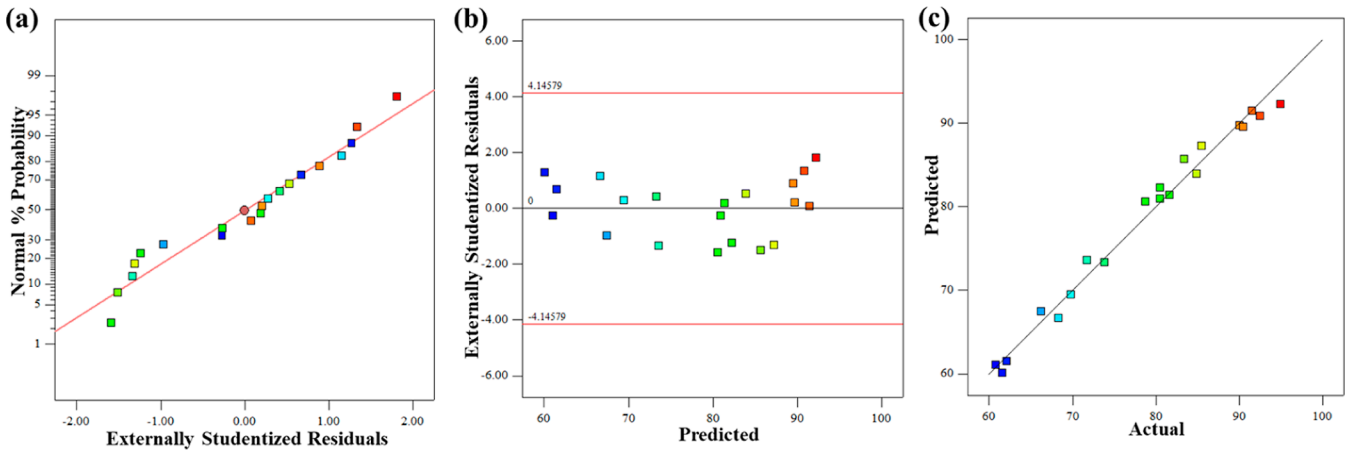

Figure 3. (a) Normal plot of residuals, (b) residuals vs predicted responses, and (c) predicted responses vs the actual values.

The ratio of the primary decomposition ratio to the secondary decomposition ratio is used to estimate the alkaline solution recovery. The decomposition ratio is determined by eq 1, and the only difference is that C_1 (g/L) is the concentration of SO_4^{2-} in L_1. Thus, the recovery ratio of alkaline solution was determined according to eq 2

$$w_{(\text{alkalinesolution})} = \frac{w_2}{w_1} \times 100\% \tag{2}$$

where w_1 (%) is the primary decomposition ratio of PG, and w_2 (%) is the secondary decomposition ratio of PG.

3. RESULTS AND DISCUSSION

3.1. Optimization of NaOH Decomposes PG by Response Surface Methodology. Since the response surface method has the advantages of less test time, high precision, and good prediction performance, many researchers have applied this method in various processes and have achieved results.[24] The central composite design model offered by Design Expert 10.0 was used in this experiment, and the response surface experiment was set with reaction temperature (A), reaction time (B), and NaOH concentration (C) as independent variables and the PG decomposition ratio as a response value. The quadratic model is selected to fit the obtained data, and the quadratic polynomial regression fitting equation of the PG decomposition ratio to the coded independent variable is obtained in eq 3

$$\begin{aligned}\text{Decomposition ratio} = {} & 94.29 + 1.56 \times A + 4.05 \times B \\ & - 3.75 \times C - 0.087 \times AB - \\ & 3.87 \times AC + 11.14 \times BC - 8.31A^2 \\ & - 0.052B^2 - 30.16C^2\end{aligned} \tag{3}$$

Table 2. ANOVA Results of the Response Surface Quadratic Polynomial Mode

source	sum of squares	mean square	F value	P-value prob > F
model	95288.64	10587.63	105.68	<0.0001
A	16.97	16.97	0.17	0.6893
B	1270.69	1270.69	12.68	0.0052
C	43561.60	43561.60	434.81	<0.0001
AB	3746.74	3746.74	37.40	0.0001
AC	0.80	0.80	7.952E-003	0.9307
BC	1388.35	1388.35	13.86	0.0040
A^2	801.26	801.26	8.00	0.0179
B^2	0.76	0.76	7.571E-003	0.9324
C^2	41.13	41.13	0.41	0.5361
residual	1001.85	100.19		

R^2 = 0.9896, R_{adj}^2 = 0.9802, pre-R^2 = 0.9338

According to the fitting equation, the responses of test values were anticipated. From Figure 3a,b, it can be seen that the normal probability distribution of the externally studentized residuals is on a straight line, the distribution of the externally studentized residuals and the predicted response values is irregular, and the actual response values of the test and the predicted response values of the model are isotropically distributed along a 45-degree diagonal line, demonstrating the model's ability to accurately and fully identify the response points.[25]

The ANOVA results showed that the model F-value was 65.79, indicating that the prespecified model was reliable (Table 2). The model P-values less than 0.0001 confirmed significant model terms. In this optimization case, several model terms such as B, BC, A^2, and C^2 were in significant form due to their less P-values. The values larger than 0.10 means insignificant model terms. In this case, A, AB, and B^2 were insignificant model terms. The R^2-value exhibited a measure of how much variability in the observed response values could be expressed by the experimental factors, as well as their interactions, by establishing a relationship between predicated and experimental consequences. R^2 close to one revealed good fitting of experimental data into predicated model equation. The regression model produced higher R^2 up to 0.9834 signifying excellent fitting between model as well as experimental data values.

The reaction surface graph, which can intuitively and vividly show better operating circumstances, is a very important step in the response surface analysis process. Figure 4 shows how temperature, time, NaOH concentration, and their interactions affect the ratio of PG decomposition. The results of response surface plots show that longer reaction times bring more adverse reactions, and the PG decomposition ratio first increases and then declines with the increase of NaOH concentration, a plane with a bent slope is formed. The explanation is that under strong alkali conditions, unnecessary

https://doi.org/10.1021/acsomega.3c07912
ACS Omega 2024, 9, 4664−4672

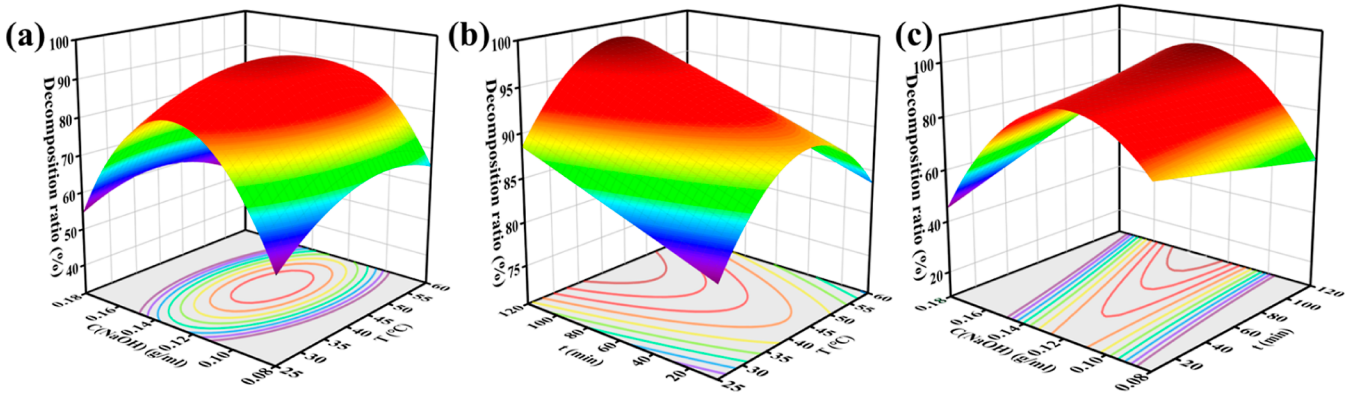

Figure 4. Response relationship between different factors to the PG decomposition ratio: (a) NaOH concentration and temperature, (b) time and temperature, and (c) NaOH concentration and time.

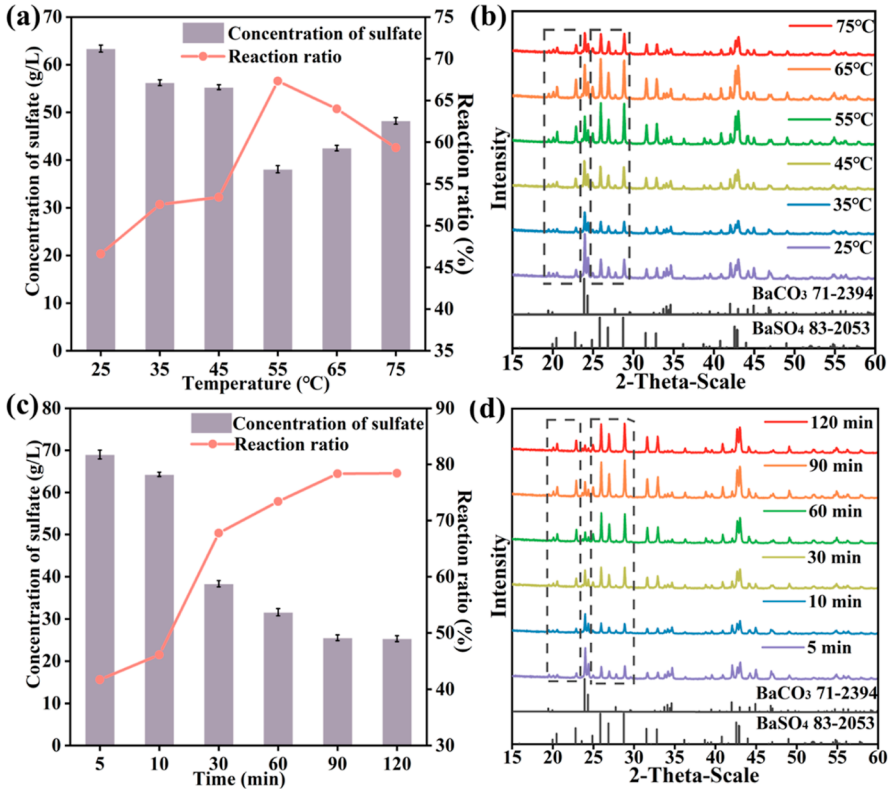

Figure 5. (a) SO_4^{2-} reaction ratio in different temperatures; (b) XRD pattern of S_2 in different temperatures; (c) SO_4^{2-} reaction ratio in different times; and (d) XRD pattern of S_2 in different times.

NaOH will react with the contamination silicate in PG to produce insoluble substances, such as $CaSiO_3$. The substance will not only consume more NaOH, but it will also increase slag in the reaction cycle, which is not conducive to the subsequent reaction. The increase in temperature will accelerate the reaction ratio. However, the side reaction between an enormous number of impurities and NaOH is an endothermic reaction. The increase in temperature is conducive to the side reaction, resulting in a decrease in the decomposition ratio of PG and an increase in the slag sum. The regression model described above was utilized to optimize the experimental parameters, and the optimal reaction condition was determined as T = 40 °C, t = 30 min, $m_{(NaOH)}/m_{(PG)}$ = 0.48:1, and $m_{(H_2O)}/m_{(PG)}$ = 4:1. The leaching ratios of Ca and S were 99.7 and 95.0%, respectively.

3.2. Conversion of $BaCO_3$ into $BaSO_4$ Based on Solubility Product Differences. According to the content of SO_4^{2-} in L_1, the amount of $BaCO_3$ is calculated. The residual SO_4^{2-} in the filtrate was used to calculate the reaction ratio. The effects of the reaction temperature and reaction time on the production of $BaSO_4$ were investigated by a single-factor experiment.

The results obtained are presented in Figure 5. According to Figure 5a, the SO_4^{2-} reaction ratio was 46.6% at 25 °C. The reaction ratio gradually increased with rising temperature. The reaction ratio of SO_4^{2-} peaked at 67.3% at 55 °C. Then, as the temperature continued to rise to 75 °C, the reaction ratio of SO_4^{2-} decreased to 59.6%. This is because, as temperature rises, the movement of molecules intensifies and the possibility of particle collision increases, which facilitates the combination

https://doi.org/10.1021/acsomega.3c07912
ACS Omega 2024, 9, 4664−4672

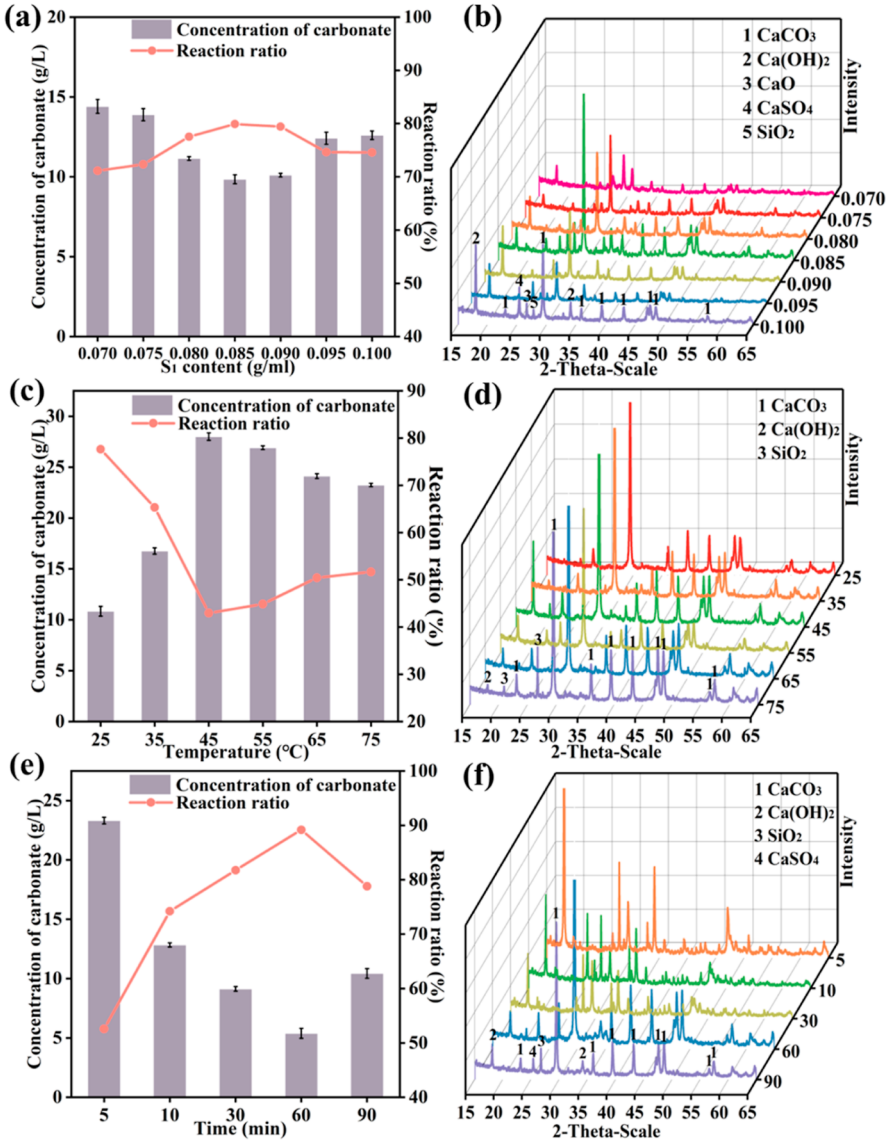

Figure 6. (a) Ca^{2+} reaction ratio in different amounts of S_1; (b) XRD pattern of S_3 in different amounts of S_1; (c) Ca^{2+} reaction ratio in different temperatures; (d) XRD pattern of S_3 in different temperatures; (e) Ca^{2+} reaction ratio in different times; and (f) XRD pattern of S_3 in different times.

of SO_4^{2-} and Ba^{2+} to form $BaSO_4$. The reaction ratio of SO_4^{2-} reduces with an increase in temperature because the solubility of Na_2SO_4 increases first before decreasing. Therefore, 55 °C was selected as the reaction temperature for producing $BaSO_4$. Figure 5c shows the impact of reaction time on the reaction ratio of SO_4^{2-} at 55 °C. As the reaction time increases, the reaction becomes more and more complete and the SO_4^{2-} reaction ratio gradually increases. The SO_4^{2-} reaction ratio was 78.3% after 90 min. The SO_4^{2-} reaction ratio did not change much after the reaction time. The XRD pattern of S_2 at different reaction temperatures and times revealed that BaSO4 was the major phase in S_2, indicating the significant dissolution of CO_3^{2-} in the filtrate and laying the foundation for the subsequent reaction of calcium particles (Figure 5b–d).

3.3. Conversion of $Ca(OH)_2$ into $CaCO_3$ Based on Solubility Product Differences. The CO_3^{2-} content present in the filtrate is used to calculate the Ca^{2+} reaction ratio. Single factor experiments were conducted to investigate the effects of the S_1 amount, reaction temperature, and reaction time on the reaction ratio of Ca^{2+}.

Figure 6a shows that the Ca^{2+} reaction ratio increased gradually with the increasing amount of the S_1 additive. The Ca^{2+} reaction ratio reached 79.9% when the S1 additive amount was 0.085 g/mL, but it decreased with higher amounts of S_1. This can mainly be attributed to the production of a supersaturated solution. The solid is difficult to dissolve at high $Ca(OH)_2$ concentrations, and this stage lasts a long time, delaying the ratio of reaction.[26] Figure 6b displays the XRD patterns of S_3 with varying amounts of the S_1 additive. It can be observed that $CaCO_3$ is the primary phase in S_3. When the amount of S_1 is 0.085 g/mL, it can be seen the XRD peak of $Ca(OH)_2$ practically disappears and $CaCO_3$ is the only phase.

Effects of the reaction temperature and time on the amount of Ca^{2+} were discussed in Figure 6, when the amount of S_1 was 0.085 g/mL. At a temperature of 25 °C, the Ca^{2+} reaction ratio was 77.6%. As the temperature increased, the ratio gradually decreased until it reached its lowest value at 45 °C, as shown in

https://doi.org/10.1021/acsomega.3c07912
ACS Omega 2024, 9, 4664−4672

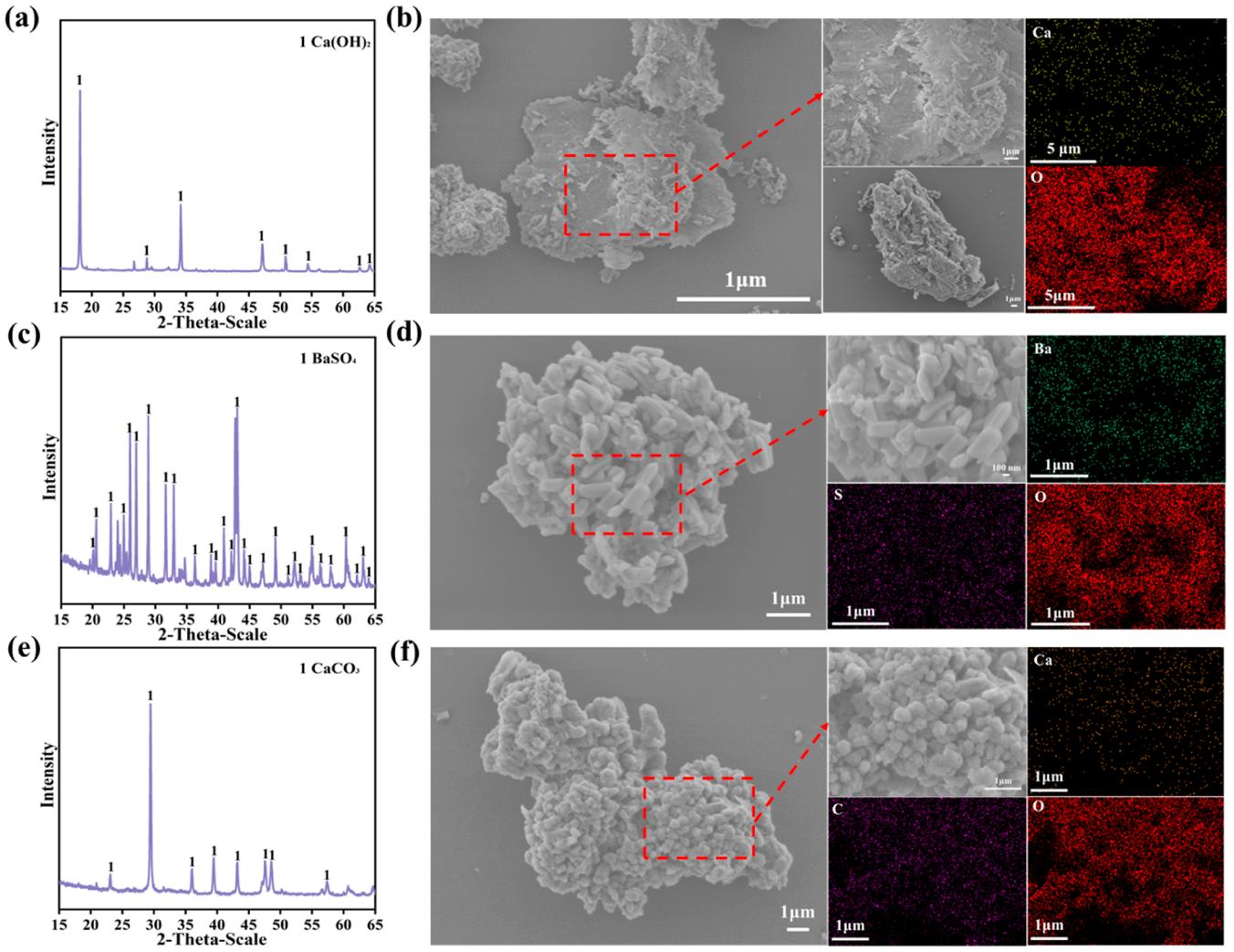

Figure 7. (a) XRD pattern of S_1, (b) SEM pattern and matching EDS data for map analysis of S_1, (c) XRD pattern of S_2, (d) SEM pattern and matching EDS data for map analysis of S_2, (e) XRD pattern of S_3, and (f) SEM pattern and matching EDS data for map analysis of S_3.

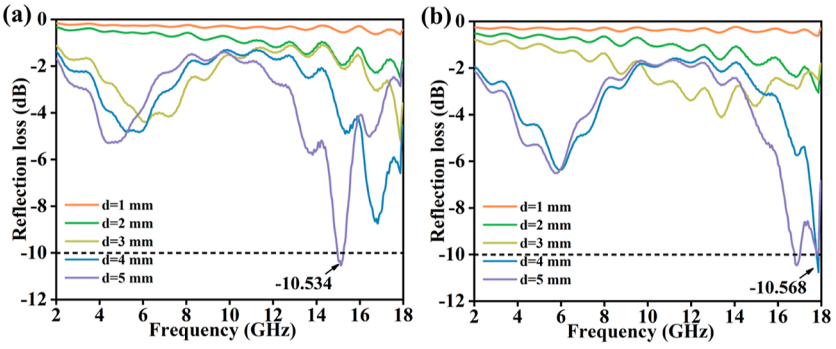

Figure 8. Reflection loss images of (a) S_2 and (b) analytical purity of $BaSO_4$.

Table 3. Contents of Part Elements from S_3 (wt %)

element	Ca	Si	Na	S	P	Fe	Al
content	48.42	4.06	12.37	1.11	0.59	0.48	0.30

Table 4. Analysis Results of Ca^{2+} and SO_4^{2-} Recovery

	theoretical value (g/L)	end of reaction (g/L)	recovery ratio (%)
Ca^{2+}	67.0	11.6×10^{-3}	99.9
SO_4^{2-}	146	25.6	82.5

Figure 6c. The reaction ratio then steadily increased and remained nearly unchanged after 65 °C because the solubility of $Ca(OH)_2$ continuously fell and its concentration steadily decreased as the reaction temperature increased. The major phase of the S_3 was $CaCO_3$ under different reaction temperatures (Figure 6d). Figure 6e illustrates the impact of the reaction time on the reaction ratio. The highest reaction ratio of 89.2% was achieved at 25 °C for a reaction time of 60

https://doi.org/10.1021/acsomega.3c07912
ACS Omega 2024, 9, 4664−4672

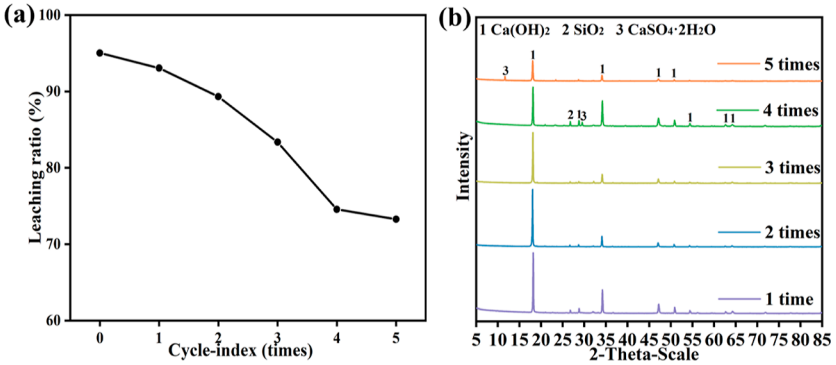

Figure 9. (a) Leaching ratio. (b) XRD pattern of the product with various cycle numbers.

min, when the S1 concentration was 0.085 g/mL. Similarly, the major phase observed for S3 at different reaction times was CaCO3, as shown in Figure 6f. $CaCO_3$ is the sole phase that exists under ideal conditions, and the peak of $Ca(OH)_2$ almost completely disappears.

3.4. Precipitation Conversion Caused by Difference in Solubility Product. In order to better explain the reaction process, we analyzed it based on the reaction equilibrium and solubility constant.

NaOH decomposes PG to produce Na_2SO_4 and $Ca(OH)_2$. The reaction is driven by the difference in solubility between $CaSO_4$ and $Ca(OH)_2$, proceeding toward the production of less soluble $Ca(OH)_2$. In Figure 7a, the main phase of the product is $Ca(OH)_2$. The SEM pattern and matching EDS data for map analysis of the product are demonstrated in Figure 7b. The reaction equation

$$CaSO_4{\cdot}2H_2O + 2NaOH = Ca(OH)_2 + Na_2CO_3 + 2H_2O \quad (4)$$

Again, depending on the difference in solubility, Na_2SO_4 in L_1 undergoes a precipitation conversion reaction with $BaCO_3$ to produce $BaSO_4$ (Figure 7c). The main morphology of the product $BaSO_4$ is fusiform (Figure 7d), and Na_2CO_3 is enriched in L_2. The reaction equation

$$Na_2SO_4 + BaCO_3 = BaSO_4 + Na_2CO_3 \quad (5)$$

Then, the $Ca(OH)_2$ in S_1 and Na_2CO_3 in L_2 engage in a precipitation conversion reaction to produce $CaCO_3$ due to the difference in solubility, and the OH^- is enriched in L_3. XRD analysis of $CaCO_3$ showed the presence only of calcite polymorph (Figure 7e). The polymorphic forms of $CaCO_3$ (aragonite and vaterite) were not identified, and the main morphology is spherical (Figure 7f). The reaction equation

$$Ca(OH)_2 + Na_2CO_3 = CaCO_3 + 2NaOH \quad (6)$$

3.5. Prospect Analysis of Products Used as Wave-Absorbing Materials. Two precipitations are obtained in the multistep precipitation, and $BaSO_4$ and $CaCO_3$ are the dominant chemical components, respectively. At present, the material containing $BaSO_4$ has a wave absorption property.[27] Tasnim et al.[28] developed the high-density shielding materials containing higher percentage (>80%) of $BaSO_4$ and their gamma-ray attenuation parameters have been investigated. The above research provides a possibility for the preparation of wave absorbances by using S_2.

The precipitations wave-absorption of S_2 qualities were evaluated. Figure 8a demonstrates the change in reflection loss value with frequency for various thicknesses (d = 1, 2, 3, 4, and 5 mm). The material's absorbing ability becomes stronger as the reflection loss value decreases. As the thickness reaches 5 mm, the reflection loss spectrum exhibits two peaks (5.00 and 15.00 GHz). The low-frequency peaks in the two peaks are connected to the displacement of the domain wall, and the high-frequency peaks are connected to the rotation of the magnetic domain, based on the understanding of magnetic physics. As the reflection loss value of the material reaches −10.00 dB, the attenuation of the absorbing material to the electromagnetic wave reaches 90%.[29] The minimum reflection loss value of S_2 is −10.53 dB. This demonstrates that S_2 precipitates, after further processing, exhibit good absorption characteristics and can be used as a radiation protective material. Furthermore, the reflection loss value of S_2 reaches 97.8% compared to the analytical purity of $BaSO_4$ (Figure 8b).

$CaCO_3$ is widely used in rubber, building materials, coatings, and other fields because of its unique physical and chemical features.[30] $CaCO_3$ is the primary phase of precipitations S_3, and the purity of the S_3 was measured to be 76.1%. The main elements in S_3 are Ca, Si, Na, and O (Table 3), which can be further used to prepare ceramics,[31] glass-ceramics,[32] or other construction industry, and further research is still underway.

3.6. Recovery of Ca and S and Alkaline Solution Recycle. The contents of residual Ca^{2+} and SO_4^{2-} in the filtrate after the reaction were measured by ICP and IC. The experimental results are displayed in Table 4. Individually, the recoveries for Ca^{2+} and SO_4^{2-} were 99.9 and 82.5%.

In order to evaluate whether the filtrate could be recovered, we conducted experiments on the recovered filtrate. Figure 9 shows the leaching ratio of SO_4^{2-} and the XRD patterns of the products for different filtrate cycle numbers. As the number of filtrate cycles increased, the leaching ratio of SO_4^{2-} gradually decreased (Figure 9a). The leaching ratio of SO_4^{2-} was 95.0% for the first cycle. After five cycles, the leaching ratio of SO_4^{2-} was 73.3%, and the alkali recovery ratio reduced from 97.9 to 77.1%. This may occur because the concentration of OH^- decreased as the cycle number increased. As demonstrated in Figure 9b, the phase of the obtained product was $Ca(OH)_2$, and as the cycle number increased, the diffraction peak corresponding to $Ca(OH)_2$ gradually weakened. After five cycles, the diffraction peak corresponding to $CaSO_4{\cdot}2H_2O$ appeared in the product.

4. CONCLUSIONS

This work successfully realized recycling Ca and S from PG in the NaOH−$BaCO_3$ system. The leaching ratio of Ca^{2+} and SO_4^{2-} in PG was 99.7 and 95.0%, respectively, under the optimized conditions (T = 40 °C, t = 30 min, $m_{(NaOH)}/m_{(PG)}$ =

https://doi.org/10.1021/acsomega.3c07912
ACS Omega 2024, 9, 4664−4672

0.48:1, and $m_{(H_2O)}/m_{(PG)}$ = 4:1). The recovery of S was 82.5% at 55 °C with a reaction time of 90 min. The recovery of Ca was 99.9% with the amount of S_1 is 0.085 g/mL, the reaction temperature is 25 °C, and a reaction time is 60 min. The product $BaSO_4$ can be used to produce wave-absorbing materials, and its reflection loss value reaches 97.8% of the analytical purity $BaSO_4$. Another product is $CaCO_3$ containing Si, Na, and O, after further treatment, which can be used in building materials industries. The alkali solution can be recycled five times, the first recovery ratio is about 97.9%, and the decomposition ratio of PG remained above 70% after five cycles. We convince that the method for PG utilization may have potential application prospect.

AUTHOR INFORMATION

Corresponding Author

Renlong Liu − *College of Chemistry and Chemical Engineering, Chongqing University, Chongqing 400044, China; State Key Laboratory of Coal Mine Disaster Dynamics and Control, Chongqing University, Chongqing 400044, China;* orcid.org/0009-0004-9591-9331; Email: lrl@cqu.edu.cn

Authors

Yuqian Zhou − *College of Chemistry and Chemical Engineering, Chongqing University, Chongqing 400044, China*

Yuhe Zhou − *School of Emergency Science, Xihua University, Chengdu 610039 Sichuan Province, China*

Guocan Zheng − *College of Chemistry and Chemical Engineering, Chongqing University, Chongqing 400044, China; Analytical and Testing Center, Chongqing University, Chongqing 400044, China*

Changyuan Tao − *College of Chemistry and Chemical Engineering, Chongqing University, Chongqing 400044, China; State Key Laboratory of Coal Mine Disaster Dynamics and Control, Chongqing University, Chongqing 400044, China*

Benjun Xi − *Hubei Three Gorges Laboratory, Yichang 443007, China*

Complete contact information is available at: https://pubs.acs.org/10.1021/acsomega.3c07912

Notes

The authors declare no competing financial interest.

ACKNOWLEDGMENTS

This work was supported by the Hubei Three Gorges Laboratory Open/Innovation Fund [grant numbers SK211009 and SK215001]; the National Key Research and Development Program of China [grant number 2019YFC1905800]; and Fundamental Research Funds for the Central Universities [grant number 2022CDJQY-005].

REFERENCES

(1) Cánovas, C. R.; Macías, F.; Pérez-López, R.; Basallote, M. D.; Millán-Becerro, R. Valorization of wastes from the fertilizer industry: Current status and future trends. *J. Cleaner Prod.* **2018**, *174*, 678−690.

(2) (a) Rashad, A. M. Phosphogypsum as a construction material. *J. Cleaner Prod.* **2017**, *166*, 732−743. (b) El Zrelli, R.; Rabaoui, L.; van Beek, P.; Castet, S.; Souhaut, M.; Grégoire, M.; Courjault-Radé, P. Natural radioactivity and radiation hazard assessment of industrial wastes from the coastal phosphate treatment plants of Gabes (Tunisia, Southern Mediterranean Sea). *Mar. Pollut. Bull.* **2019**, *146*, 454−461.

(3) (a) Guerrero, J. L.; Pérez-Moreno, S. M.; Gutiérrez-Álvarez, I.; Gázquez, M. J.; Bolívar, J. P. Behaviour of heavy metals and natural radionuclides in the mixing of phosphogypsum leachates with seawater. *Environ. Pollut.* **2021**, *268*, 115843. (b) Kuzmanović, P.; Todorović, N.; Forkapić, S.; Petrović, L. F.; Knežević, J.; Nikolov, J.; Miljević, B. Radiological characterization of phosphogypsum produced in Serbia. *Radiat. Phys. Chem.* **2020**, *166*, 108463.

(4) Fei, X.; Fang, M.; Wang, Y. Climate change affects land-disposed waste. *Nat. Clim. Change* **2021**, *11* (12), 1004−1005. Letter

(5) (a) Huang, Y.; Qian, J.; Lu, L.; Zhang, W.; Wang, S.; Wang, W.; Cheng, X. Phosphogypsum as a component of calcium sulfoaluminate cement: Hazardous elements immobilization, radioactivity and performances. *J. Cleaner Prod.* **2020**, *248*, 119287. (b) Wang, F.; Xu, J.; Yin, H.; Zhang, Y.; Pan, H.; Wang, L. Sustainable stabilization/solidification of the Pb, Zn, and Cd contaminated soil by red mud-derived binders. *Environ. Pollut.* **2021**, *284*, 117178.

(6) Ma, B.; Jin, Z.; Su, Y.; Lu, W.; Qi, H.; Hu, P. Utilization of hemihydrate phosphogypsum for the preparation of porous sound absorbing material. *Constr. Build. Mater.* **2020**, *234*, 117346.

(7) Michalovicz, L.; Müller, M. M. L.; Tormena, C. A.; Dick, W. A.; Vicensi, M.; Meert, L. Soil chemical attributes, nutrient uptake and yield of no-till crops as affected by phosphogypsum doses and parceling in southern Brazil. *Arch. Agron Soil Sci.* **2019**, *65* (3), 385−399. Article

(8) Li, X.; Zhang, Q. Effect of Molecular Structure of Organic Acids on the Crystal Habit of alpha- $CaSO_4{\cdot}0.5H_2O$ from Phosphogypsum. *Crystals* **2020**, *10* (1), 130114. Article

(9) Ennaciri, Y.; Alaoui-Belghiti, H. E.; Bettach, M. Comparative study of K_2SO_4 production by wet conversion from phosphogypsum and synthetic gypsum. *J. Mater. Res. Technol.* **2019**, *8* (3), 2586−2596.

(10) Li, L.; Liao, L.; Wang, B.; Li, W.; Liu, T.; Wu, P.; Xu, Q.; Liu, S. Effective Sb(V) removal from aqueous solution using phosphogypsum-modified biochar. *Environ. Pollut.* **2022**, *301*, 119032.

(11) Zhao, L.; Zhang, Q.; Li, X.; Ye, J.; Chen, J. Adsorption of Cu(II) by phosphogypsum modified with sodium dodecyl benzene sulfonate. *J. Hazard. Mater.* **2020**, *387*, 121808.

(12) (a) Chen, Q.; Ding, W.; Sun, H.; Peng, T.; Ma, G. Utilization of Phosphogypsum to Prepare High-Purity $CaCO_3$ in the NH_4Cl-NH_4OH-CO_2 System. *ACS Sustain. Chem. Eng.* **2020**, *8* (31), 118148−211657. Article (b) Chen, Q.; Ding, W.; Sun, H.; Peng, T.; Ma, G. Indirect mineral carbonation of phosphogypsum for CO_2 sequestration. *Energy* **2020**, *206*, 118148.

(13) (a) He, H.; Hao, L.; Fan, C.; Li, S.; Lin, W. A two-step approach to phosphogypsum decomposition: Oxidation of CaS with CO_2. *Thermochim. Acta* **2022**, *708*, 179122. (b) Sun, L.; Zhao, Z.; Yang, X.; Sun, Y.; Li, Q.; Luo, C.; Zhao, Q. Thermochemical decomposition of phosphogypsum with Fe-P slag via a solid-state reaction. Chin. *J. Chem. Eng.* **2022**, *47*, 113−119.

(14) (a) Wei, J.; Gu, Y.; Lv, H.; Wu, X. A zero-emission method for recycling phosphogypsum using Na_2SO_4 electrolysis: Preliminary study. *Sep. Purif. Technol.* **2021**, *259*, 118168. (b) Zhou, J.; Gao, H.; Shu, Z.; Wang, Y.; Yan, C. Utilization of waste phosphogypsum to prepare non-fired bricks by a novel Hydration-Recrystallization process. *Constr. Build. Mater.* **2012**, *34*, 114−119.

(15) Li, J.; Peng, X.; Zheng, J.; Mao, M.; Sun, X.; Wang, J.; Li, X.; Chai, X.; Lin, Z.; Liu, W. Simultaneous removal of phosphorus and organic contaminants from phosphogypsum using hydrothermal method for gypsum resource regeneration. *J. Environ. Chem. Eng.* **2022**, *10* (5), 108441.

(16) Ding, W.; Chen, Q.; Sun, H.; Peng, T. Modified mineral carbonation of phosphogypsum for CO_2 sequestration. *J. CO_2 Util.* **2019**, *34*, 507−515.

(17) Onoda, H.; Iinuma, A. Selective preparation of neodymium phosphates from iron mixed solution by two-step precipitation. *J. Environ. Chem. Eng.* **2020**, *8* (5), 104083.

(18) Xia, L.; Zhang, W.; Che, J.; Chen, J.; Wen, P.; Ma, B.; Wang, C. Stepwise removal and recovery of phosphate and fluoride from

https://doi.org/10.1021/acsomega.3c07912
ACS Omega 2024, 9, 4664−4672

wastewater via pH-dependent precipitation: Thermodynamics, experiment and mechanism investigation. *J. Cleaner Prod.* **2021**, *320*, 128872.
(19) (a) Shu, J.; Wu, H.; Chen, M.; Peng, H.; Li, B.; Liu, R.; Liu, Z.; Wang, B.; Huang, T.; Hu, Z. Fractional removal of manganese and ammonia nitrogen from electrolytic metal manganese residue leachate using carbonate and struvite precipitation. *Water Res.* **2019**, *153*, 229−238. (b) Shu, J.; Cai, L.; Zhao, J.; Feng, H.; Chen, M.; Zhang, X.; Wu, H.; Yang, Y.; Liu, R. A low cost of phosphate-based binder for Mn^{2+} and NH^{4+}-N simultaneous stabilization in electrolytic manganese residue. *Ecotoxicol. Environ. Saf.* **2020**, *205*, 111317.
(20) Borai, E.; El Afifi, E.; Shahr El-Din, A. Selective elimination of natural radionuclides during the processing of high grade monazite concentrates by caustic conversion method. *Korean J. Chem. Eng.* **2017**, *34*, 1091−1099.
(21) Swanepoel, H.; de Beer, M.; Liebenberg, L. Complete sulphate removal from neutralised acidic mine drainage with barium carbonate. *Water Pract. Technol.* **2012**, *7* (1), wpt2012003.
(22) Ashekuzzaman, S. M.; Jiang, J.-Q. Study on the sorption-desorption-regeneration performance of Ca-Mg- and CaMg-based layered double hydroxides for removing phosphate from water. *Chem. Eng. J.* **2014**, *246*, 97−105.
(23) Wei, Y.; Sun, R.; Su, H.; Xu, H.; Zhang, L.; Huang, D.; Liang, Z.; Hu, Y.; Zhao, L.; Lian, X. Synthesis and characterization of porous $CaCO_3$ microspheres templated by yeast cells and the application as pH value-sensitive anticancer drug carrier. *Colloids Surf., B* **2021**, *199*, 111545.
(24) Basha, C. A.; Saravanathamizhan, R.; Manokaran, P.; Kannadasan, T.; Lee, C. W. Photoelectrocatalytic Oxidation of Textile Dye Effluent: Modeling Using Response Surface Methodology. *Int. J. Miner. Process.* **2012**, *51* (7), 2846−2854.
(25) (a) Peng, H.; Guo, J.; Qiu, H.; Wang, C.; Zhang, C. Degradation of sulfamethazine sodium salt by peroxymonosulfate activated by biochar supported $CoFe_2S_4$: Performance, mechanism and response surface method optimization. *J. Environ. Chem. Eng.* **2022**, *10* (5), 889. (b) Hao, Z.; Rao, Y.; Gong, Y.; Wang, C.; Zhang, C.; Hao, Z.; Rao, Y.; Gong, Y. Efficient Removal of Cr (VI) with Biochar and Optimized Parameters by Response Surface Methodology. *Processes* **2021**, *9* (5), 889.
(26) Bouargane, B.; Marrouche, A.; El Issiouy, S.; Biyoune, M. G.; Mabrouk, A.; Atbir, A.; Bachar, A.; Bellajrou, R.; Boukbir, L.; Bakiz, B. Recovery of $Ca(OH)_2$, $CaCO_3$, and Na_2SO_4 from Moroccan phosphogypsum waste. *J. Mater. Cycles Waste Manag.* **2019**, *21* (6), 1563−1571. Article
(27) (a) Mann, K. S.; Heer, M. S.; Rani, A. Investigation of clay bricks for storage facilities of radioactive-wastage. *Appl. Clay Sci.* **2016**, *119*, 249−256. (b) Souza, G. A. G. R.; Sigifredo Cortés Paredes, R.; Saicla Barros, F.; Bavaresco Sucharski, G.; Ribeiro Junior, S.; Dalmaso Neto, C.; Ribas Santos, L.; Ferreira Ńtchalá, W.; Bavaroski Toledo Costa, F. Characterization of a coating for radioprotection, by X-ray diffraction, scanning electron microscopy, and dispersive energy spectroscopy. *Constr. Build. Mater.* **2022**, *321*, 126326.
(28) Tasnim, A.; Sahadath, M. H.; Islam Khan, M. N. Development of high-density radiation shielding materials containing $BaSO_4$ and investigation of the gamma-ray attenuation properties. *Radiat. Phys. Chem.* **2021**, *189*, 109772.
(29) (a) Tao, J.; Zhou, J.; Yao, Z.; Jiao, Z.; Wei, B.; Tan, R.; Li, Z.; Bin Hamid, M. A. Optimization of magnetite with modified graphene for microwave absorption properties. *J. Alloys Compd.* **2023**, *936*, 542. (b) Tao, J.; Zhou, J.; Yao, Z.; Jiao, Z.; Wei, B.; Tan, R.; Li, Z. Multi-shell hollow porous carbon nanoparticles with excellent microwave absorption properties. *Carbon* **2021**, *172*, 542−555.
(30) (a) Kuo, D.; Nishimura, T.; Kajiyama, S.; Kato, T. Bioinspired Environmentally Friendly Amorphous $CaCO_3$-Based Transparent Composites Comprising Cellulose Nanofibers. *ACS Omega* **2018**, *3* (10), 12722−12729. (b) Xu, J.; Wang, X.; Wang, B. Biochemical process of ureolysis-based microbial $CaCO_3$ precipitation and its application in self-healing concrete. *Appl. Microbiol. Biotechnol.* **2018**, *102* (7), 3121−3132.
(31) Salomão, R.; Ferreira, V. L.; de Oliveira, I. R.; Souza, A. D. V.; Correr, W. R. Mechanism of pore generation in calcium hexaluminate (CA6) ceramics formed in situ from calcined alumina and calcium carbonate aggregates. *J. Eur. Ceram. Soc.* **2016**, *36* (16), 4225−4235.
(32) Brentrup, G. J.; Moawad, H. M. M.; Santos, L. F.; Almeida, R. M.; Jain, H. Structure of Na_2O-CaO-P_2O_5-SiO_2 Glass-Ceramics with Multimodal Porosity. *J. Am. Ceram. Soc.* **2009**, *92* (1), 249−252.

https://doi.org/10.1021/acsomega.3c07912
ACS Omega 2024, 9, 4664−4672